Research Article Vol. 59, No. 13 / 1 May 2020 / Applied Optics D125

Single-shot phase calibration of a spatial light modulator using geometric phase interferometry

Luke A. DeMars,[1,†] Marta Mikuła-Zdańkowska,[1,2,†] Konstantinos Falaggis,[1] and Rosario Porras-Aguilar[1,*]

[1]University of North Carolina at Charlotte, 9201 University City Blvd., Charlotte, North Carolina 28223, USA
[2]Warsaw University of Technology, Faculty of Mechatronics, Institute of Micromechanics and Photonics, 8 Sw. Andrzeja Boboli Street, 02-525 Warsaw, Poland
*Corresponding author: rporrasa@uncc.edu

Received 19 November 2019; revised 23 January 2020; accepted 7 February 2020; posted 10 February 2020 (Doc. ID 383610); published 13 March 2020

A vibration-insensitive, single-shot phase-calibration method for phase-only spatial light modulators (SLM) is reported. The proposed technique uses a geometric phase lens to form a phase-shifting radial shearing interferometer to enable common-path measurements. This configuration has several advantages: (a) unlike diffraction-based SLM calibration techniques, this technique is robust against intensity errors due to misalignment; (b) unlike two-beam interferometers, this technique offers a high environmental stability; and (c) unlike intensity-based methods, the phase-shifting capability provides a phase uncertainty routinely in the order of $2\pi/100$. The experimental results show a significantly higher accuracy when compared to the diffraction-based approaches.

https://doi.org/10.1364/AO.383610

1. INTRODUCTION

Phase-only liquid-crystal-on-silicon spatial light modulator (SLM) technology has become a popular solution in a wide range of optical applications as programmable optical devices [1,2] ranging from interferometry [3] and imaging through scattering media [4] to the generation of structured beams [5]. Furthermore, SLMs provide an active solution that can correct for sources of error in the generation of wavefronts, especially aberration correction of the measurement system using phase modulation [6–8]. With this variety of applications in mind, the phase distribution provided by an SLM must be characterized and calibrated to provide an accurate phase modulation. Several calibration techniques have been reported that can be categorized as interferometric, diffractive, and polarization-based measurements [9,10]. For the sake of brevity, we have included only exemplary publications to represent the main categories. Interferometric methods involve the use of self-reference methodologies, where a portion of the SLM serves as the reference [11] and out-referenced implementations (basically Twyman–Green configurations, which in combination with piezo-electric devices and phase-shifting algorithms [12], provide an accurate phase measurement). Diffractive methods rely on grating models to relate the phase projected on the SLM to the intensity measured in either a Fourier plane [13] or other detection planes; see, for example [14–16]. Diffraction-based methods offer a simple solution that includes local and global measurements of the SLM panel. However, they lack accuracy compared to phase-shifting interferometric methods. Also, diffraction-based methods present a significant experimental disadvantage, which is the uncertainty of the placement of the sensor at a precise distance from the SLM, which results in inaccurate intensity measurements. On the other hand, polarization methods use polarimetric measurements such as the Mueller matrix [17] or the Stoke parameters [18] to calculate the phase retardance. Recently, another novel approach was the use of a cross-analyzer system to relate the phase to intensity or to be used as a phase shifter [19]. In general, these methodologies are robust; however, they require several measurements to calculate the phase retardance.

In this paper, we describe a method that uses a geometric phase (GP) lens in a configuration that produces radially sheared interferograms to measure gamma nonlinearity of the SLM [19]. GP lenses have been exploited in recent studies of incoherent digital holography [20–22]. The calibration system proposed here differentiates from previous methodologies as for being (1) a single-shot phase measurement and (2) a common-path configuration. This is an advantage in comparison to most calibration techniques that require a minimum of four images [9]. Also, contrary to conventional interferometric methods, the common-path configuration allows for measurements that are robust to vibrations. Moreover, alignment complexity was significantly reduced in the presented method in comparison

to off axis as, e.g., diffractive methods [13,15] or methods that require multiple-path optical setups [23–25]. In addition to these benefits, these GP lenses are cost effective and have become off-the-shelf components in recent years.

The paper is organized as follows. Section 2 describes the fundamental principles of the GP lens. Section 3 shows the calibration system used in the measurement of the gamma curve and the analysis process. Section 4 is the discussion of the phase measurements attained and the gamma curve. Section 5 includes the conclusion and final remarks.

2. GEOMETRIC PHASE AND THE GEOMETRIC PHASE LENS

Geometric phase lenses are flat liquid crystal patterned optical elements that, due to their optical anisotropy, can act as either a converging or diverging lens depending on the input polarization; see Fig. 1 [26]. The focal length f of a GP lens is wavelength dependent [27–29].

Also known as the Pancharatnam–Berry phase, the geometric phase device's working principle is based on a local modification of the polarization state traveling through the optical element [27]. If the incoming illumination is linearly polarized, then the converging and diverging wavefront have right-handed circular polarization and left-hand circular polarization, respectively [21].

As described in Refs. [21,22], the intensity pattern captured when a polarizer of arbitrary angle Ω is placed between the GP lens and a camera is given by Eq. (1), where $\pm\Phi$ is the quadratic phase modulation (as a positive and negative lens) of the GP lens:

$$I(x, y) = I_o(x, y) + I_o(x, y)\cos(2\Omega + 2\Phi_{\mathrm{SLM}}). \quad (1)$$

In other words, by rotating the polarizer, it is possible to obtain four intensity distributions that can be employed in a phase-shifting algorithm. The calibration method presented here is based on the use of those intensity distributions (holograms). A polarized camera with an on-sensor array of linear polarizers [30] (at four different polarizations) was used to capture four phase-shifted intensities simultaneously and to calculate the phase with a single shot.

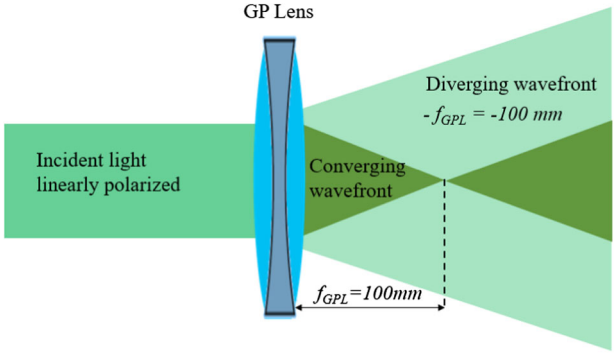

Fig. 1. GP lens with incident linearly polarized light splitting the wavefront into both a diverging and converging wavefront.

3. CALIBRATION SYSTEM AND MEASUREMENT METHODOLOGY

A. Experimental Setup

The calibration system for measuring the nonlinearity of the gamma curve is shown in Fig. 2. Here the beam is generated by monochromatic laser illumination ($\lambda = 532$ nm) that is filtered and collimated. The beam has a diameter of approximately 8 mm and is linearly polarized with the fast axis of the SLM by means of a half-wave plate (HWP). A non-polarizing beam splitter allows for normal incident light to be modulated by the SLM. The SLM under test was the Holoeye Pluto 2 VIS-16 with high phase retardation (6.7π for 532 nm, pixel pitch 8 μm, resolution 1920 × 1080, fill factor of 93%, and dimension of 15.36 mm × 8.64 mm). The reflected light is redirected towards the radial shearing interferometer (RSI), which is the central part of our calibration system. The RSI consists of the GP lens (diameter of 25.4 mm and focal length of 100 mm for 532 nm) and a converging relay lens (diameter of 25.4 mm and focal length of 100 mm). The total length of this system forms a $4f$ system with unitary magnification for the object wave. The RSI working principle is that the optical path length difference is generated by varying the radii of the two wavefronts [31–33].

Then the radially sheared interferogram is captured by a polarization camera (FLIR BFS-U3-51S5P-C, pixel size 3.45 μm × 3.45 μm, resolution 2448 × 2048, and dimensions of 8.80 mm × 6.60 mm), which is placed at the focal length of the relay lens. The polarized camera is fabricated with an on-sensor array of linear polarizers in four different orientations (0, 45, 90, and 135 deg) [30]. This array of linear polarizers allows for four phase-shifted interferograms (each using a $^1/_4$ of the total amount of pixels) to be captured simultaneously and therefore enabling single-shot phase measurements. The phase difference at the SLM (Φ_{SLM}) is calculated using Eq. (2) [12,21]:

$$\Phi_{\mathrm{SLM}} = \tan^{-1}\left(\frac{I(x, y, 135°) - I(x, y, 45°)}{I(x, y, 0°) - I(x, y, 90°)}\right). \quad (2)$$

B. Measurement of the Gamma Curve

The SLM calibration requires determination of the relationship between the grey level sent to the SLM and the phase modulation. For this purpose, the SLM was programmed with a phase

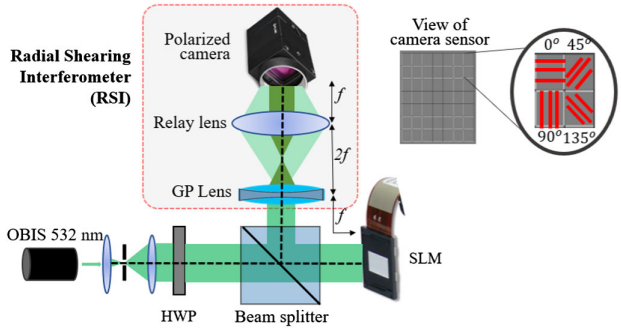

Fig. 2. Calibration system to measure gamma nonlinearity of SLM. The radial shearing interferometer (RSI) is shown in the dashed square. It consists of a GP lens, a relay lens, and a polarized camera.

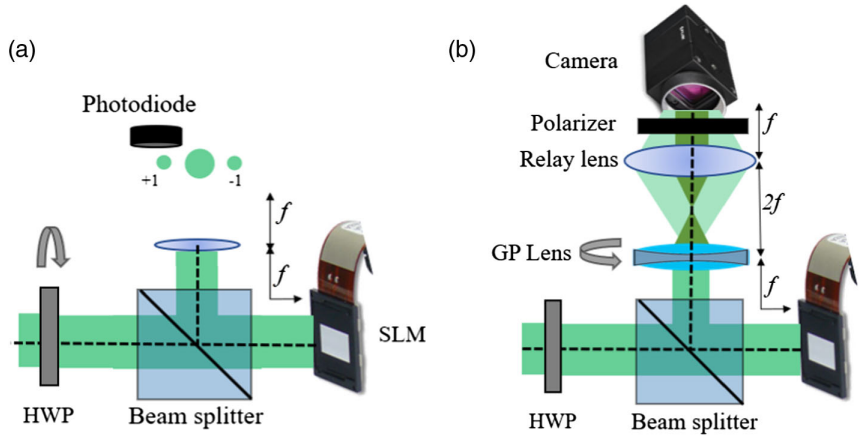

Fig. 3. (a) Alignment process of the SLM fast axis with the incident polarization and (b) optimization of the GP lens fringe visibility.

reference distribution (grey level equals zero along the SLM), and the phase difference was calculated in comparison with a binary phase object at the SLM for each grey level. This phase object is projected sequentially in steps of 1 from 1 to 255, and a series of object holograms is collected at each step. Then, using Eq. (2), the phase for both the reference and the object holograms are solved.

In order to align the linear polarization of the light both, with the SLM fast axis and the optimal orientation of the GP lens, the following procedure was taken. First, the linearly polarized light was rotated with a half-wave plate and aligned with the fast axis of the SLM. Alignment with the SLM fast axis was made by projecting a binary grating onto the SLM and then measuring the power with a photodiode in the first diffraction order in the far field with the aid of a Fourier transform lens. The half-wave plate was rotated to maximize the power in the first order of diffraction as shown in Fig. 3(a). In the second step, the GP lens was placed on a continuous rotation mount about the optical axis as shown in Fig. 3(b). The GP lens's angular position was determined by maximizing the visibility fringes observed by placing a polarizer in front of a conventional camera.

After aligning the linear polarization of the system with the fast axis of the SLM [Fig. 3(a)] and optimizing the orientation of the GP lens [Fig. 3(b)], vertically incident polarized light is transmitted into the GP lens, which splits the light both into right- and left-hand circularly polarized light. The camera and polarizer were replaced by a polarized camera, as shown in Fig. 2, where four polarization states were captured in a single shot (0, 45, 90, and 135 deg) and processed to calculate the phase retardance.

4. PHASE DATA, GAMMA CURVE, AND DISCUSSION

For the gamma curve determination, the square of 100 pixels × 100 pixels pixels was chosen as an object. During the measurement, the grey level of the square was changed in the range from 0 to 255. Note that PLUTO-2-VIS-016 enables us to change the phase up to 6.7π at 530 nm wavelength. However, the retrieved phase is within a range from $-\pi$ to π because of the 2π ambiguity of the wrapped phase [34]. This means that for the entire calculation of the gamma curve to 6.7π, we obtained the repetition of phase information for each 2π period. Therefore, at each point of discontinuity in the gamma, a multiple of 2π was added to represent the correct phase value.

The registered holograms show the presence of a twin image (i.e., a virtual image), which is a defocused image of the measured object, and the speckle-noise effect because of the high-coherence light source (monochromatic laser). The twin image problem is considered a limitation of the holographic techniques.

Due to the nature of the GP lens being self-referencing, a copy of the object is made in the reference wave. Because of the imaging conditions set by the calibration system, this copy is unfocused and is highly diffracted. To limit undesired diffraction effects from this unfocused copy, the object was placed at an off-axis location so that the twin and the object do not overlap as shown in Fig. 4. The off-axis distance was calculated to be 3.8 mm from the center of the phase object to the center of the SLM. However, the diffractive effects still affect the result of the final phase. Figures 5(a)–5(c) show five different retrieved phases without any filtration; the selected grey levels of the objects are the following: 10, 20, 40, 100, and 200. Due to the spatial separation of the twin image and phase object, which is shown in Fig. 4, there is no need to apply the iterative phase-retrieval method to suppress the twin image [35].

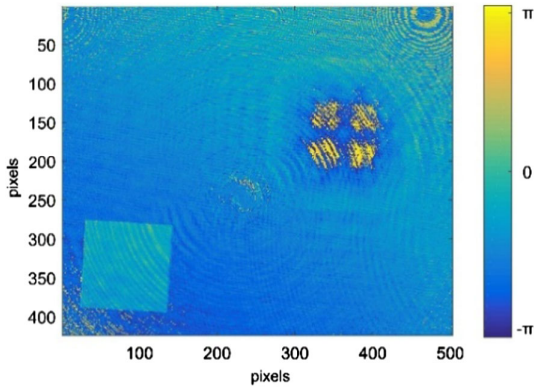

Fig. 4. Presence of twin image phase map for a grey level of 200. Spatial separation of the twin image and phase object.

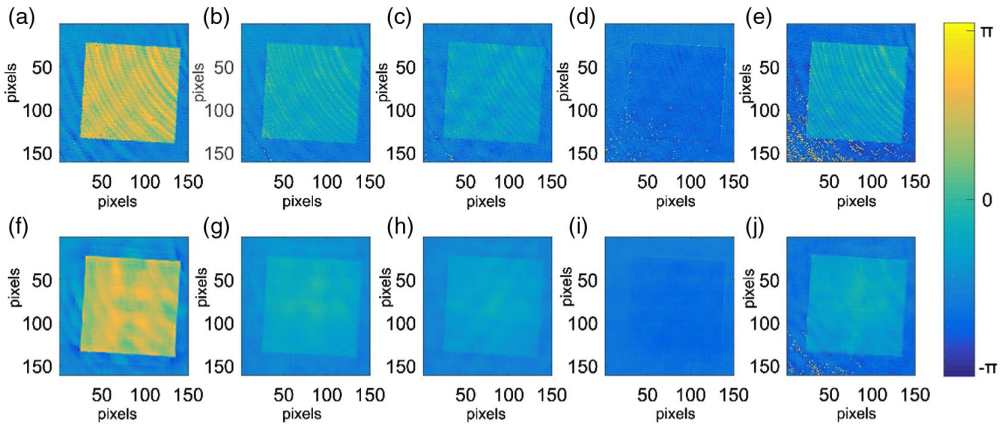

Fig. 5. Retrieved phases (a)–(e) without any filtration and (f)–(j) filtrated using the proposed procedure of the selected grey levels of the objects: (a), (f) 10; (b), (g) 20; (c), (h) 40; (d), (i) 100; and (e), (j) 200.

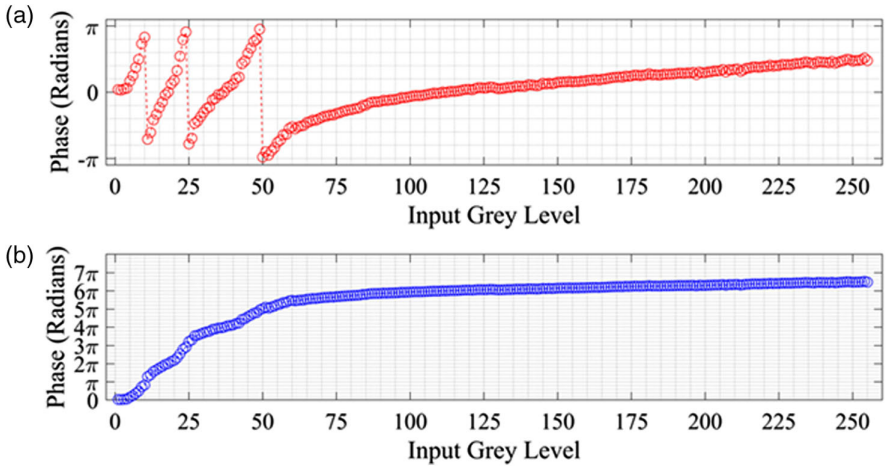

Fig. 6. Experimentally obtained gamma curve of the Holoeye Pluto 2 V16: (a) the wrapped gamma curve due to large modulation in the device and (b) the unwrapped gamma curve.

Table 1. Quantitative Comparison between Results Obtained with and without Filtration Procedure

Grey Level	10	20	40	100	200
σ before filtration	0.475	0.341	0.307	0.282	0.395
σ after filtration	0.118	0.107	0.079	0.091	0.064

In our approach, the twin image and noise suppression are done by the following steps: (1) filtering each retrieved phase using the block-matching 3D (BM3D) image denoising method [36–38]; (2) propagating the optical field [39,40] to obtain the focused twin image; (3) applying a Gaussian filter of part of the hologram with the twin image; (4) backpropagation of the optical field to the focused object image. The propagation in Figs. 5(d)–5(f) shows the retrieved phases after filtration by the proposed procedure. It can be noticed that the effects of the parasitic fringes and speckle noise are suppressed. Table 1 presents a quantitative comparison between the results obtained with and without the proposed filtration procedure. The calculated σ of the retrieved phase confirms that the method we proposed works properly, as a clear reduction of parasitic effects can be observed.

In Fig. 6, the estimate of the gamma curve is shown. The obtained data is in agreement with the specifications provided by the manufacturers at 530 nm, approximately 6.7π of phase retardation.

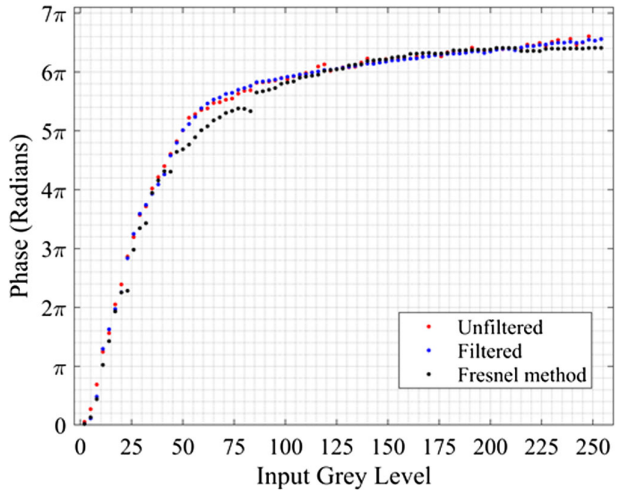

Fig. 7. Measured gamma curve using: unfiltered data (red), filtered data (blue), and the referenced Fresnel method (black).

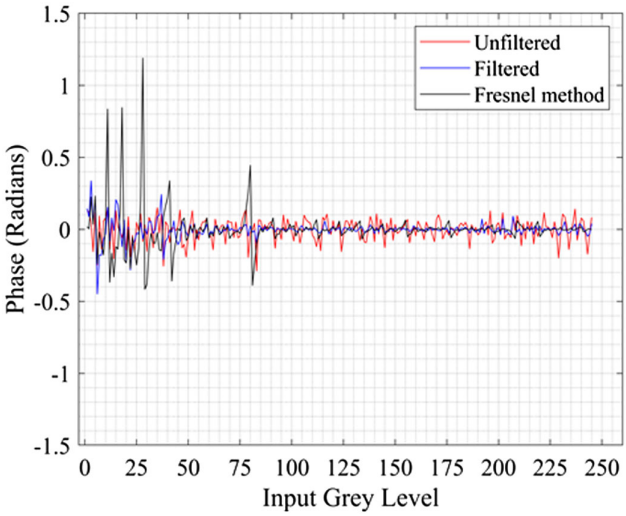

Fig. 8. Moving average of each measured gamma curve using: unfiltered data (red), filtered data (blue), and the referenced Fresnel method (black).

Figure 7 shows the measured relation between phase and grey level (so-called gamma curve) using: (1) unfiltered data (blue line), (2) filtered data (red line), and (3) for reference we have included the gamma curve obtained using a diffraction-based methodology (black line) [14]. It can be noticed that the filtered and unfiltered data are similar. The obtained data is in agreement with the specifications provided by the manufacturers at 530 nm, approximately 6.7π of phase retardation for all methodologies. Notably, the measurements obtained with the Fresnel method show to have significant outliners and discontinuities, which highlight an inherent weakness of diffraction-based methods. Furthermore, the graph in Fig. 7 can further be improved using sophisticated regression techniques; however, this is beyond the scope of this work.

To estimate the uncertainty level of the GP lens method proposed here, we calculated the moving average of each curve, which is shown in Fig. 8, and the standard deviation, which was found to be 0.14, 0.08, and 0.06 for the Fresnel method, unfiltered data, and filtered data, respectively. Based on these calculations, the uncertainty for the filtered data is $\sim \lambda/100$ or $(2\pi/100 = 0.06$ rad).

In addition to our results, we show in Table 2 a list of ideal traits that SLM calibration methods have—listing the three main categories, including interferometric, diffraction, and polarization base calibrations. Our approach using a GP lens and a polarization camera falls under the categories of polarization and interferometric, resulting in an accurate, single-shot phase-calibration methodology.

5. SUMMARY

In summary, a single-shot polarization-based calibration technique for phase-only SLMs was described here. With the use of a GP lens paired with a polarized camera, a phase-shifting radial shearing interferometer was built to calibrate the phase modulation of an SLM. A gamma curve was generated that meets the specifications of the manufacturer. This calibration procedure uses a common-path configuration that is insensitive to environmental disturbances. The alignment requirements of this setup are less stringent than interferometric and grating-based methods. Taking advantage of the interference of waves, the phase at each grey level is estimated with an interferometric phase-shifting technique that provides a phase uncertainty in the order of $2\pi/100$, despite the presence of the twin image.

Table 2. List of Advantages and Disadvantages of SLM Calibration Methods

Methodology		Exemplary References	Advantages	Disadvantages
Interferometry	Self-reference	[11]	Simple setup	Not accurate It does not provide localized measurements
	Two-beam interferometry	[23,25]	High accuracy, when combined with phase-shifting algorithms.	Requires a flat reference
	Digital holography		Provides global and local phase measurements	Sensitive to vibrations and temperature changes
Diffraction		[13–16]	Provides global and local phase measurements Simple calculation from intensity to phase	Distance uncertainty, thus low accurate Not applicable for phase-shifting algorithms
Polarization		[17,18,24,41]	Local measurements High accuracy, when combined with phase-shifting algorithms	Requires from four to several measurements
GP Lens		This approach	Single-shot phase measurement Robust common-path configuration Easy alignment High accuracy, when combined with phase-shifting algorithms	Global measurements are limited by the presence of the twin image but can be obtained with sequential measurements (placing the object at different locations)

Funding. University of North Carolina at Charlotte; Polish National Agency for Academic Exchange (PROM Project CWW/PROM PW/2019/029).

Acknowledgment. This work was supported, in part, by funds provided by the University of North Carolina at Charlotte. M. M. Z. acknowledges support from PROM project CWM/PROM PW/2019/029 funded by the Polish National Agency for Academic Exchange.

[†]These authors contributed equally to this work.

REFERENCES

1. M. Kujawińska, R. Porras-Aguilar, and W. Zaperty, "LCoS spatial light modulators as active phase elements of full-field measurement systems and sensors," Metrol. Meas. Syst. **19**, 445–458 (2012).
2. C. Maurer, A. Jesacher, S. Bernet, and M. Ritsch-Marte, "What spatial light modulators can do for optical microscopy," Laser Photon. Rev. **5**, 81–101 (2011).
3. J. Kacperski and M. Kujawinska, "Active, LCoS based laser interferometer for microelements studies," Opt. Express **14**, 9664–9678 (2006).
4. I. M. Vellekoop and A. P. Mosk, "Focusing coherent light through opaque strongly scattering media," Opt. Lett. **32**, 2309–2311 (2007).
5. J. Mendoza-Hernández, M. Szatkowski, M. F. Ferrer-Garcia, J. C. Gutiérrez-Vega, D. Lopez-Mago, J. C. Gutiérrez-Vega, D. Lopez-Mago, and D. Lopez-Mago, "Generation of light beams with custom orbital angular momentum and tunable transverse intensity symmetries," Opt. Express **27**, 26155–26162 (2019).
6. J. L. Martinez, E. J. Fernandez, P. M. Prieto, and P. Artal, "Chromatic aberration control with liquid crystal spatial phase modulators," Opt. Express **25**, 9793–9801 (2017).
7. F. Vargas-Martín, P. M. Prieto, and P. Artal, "Correction of the aberrations in the human eye with a liquid-crystal spatial light modulator: limits to performance," J. Opt. Soc. Am. A **15**, 2552–2562 (1998).
8. E. J. Fernández, P. M. Prieto, and P. Artal, "Wave-aberration control with a liquid crystal on silicon (LCOS) spatial phase modulator," Opt. Express **17**, 11013–11025 (2009).
9. R. Li and L. Cao, "Progress in phase calibration for liquid crystal spatial light modulators," Appl. Sci. **9**, 2012 (2019).
10. A. E. M. Browar, M. Shusteff, B. E. Kelly, R. M. Panas, J. D. Ellis, and C. M. Spadaccini, "Overview and comparison of spatial light modulator calibration methods," in *Proceeding—ASPE 2016 Annual Meeting* (2016), pp. 293–299.
11. Z. Zhao, Z. Xiao, Y. Zhuang, H. Zhang, and H. Zhao, "An interferometric method for local phase modulation calibration of LC-SLM using self-generated phase grating," Rev. Sci. Instrum. **89**, 083116 (2018).
12. K. Creath, "V phase-measurement interferometry techniques," Prog. Opt. **26**, 349–393 (1988).
13. E. Ronzitti, M. Guillon, V. de Sars, and V. Emiliani, "LCoS nematic SLM characterization and modeling for diffraction efficiency optimization, zero and ghost orders suppression," Opt. Express **20**, 17843–17855 (2012).
14. O. Mendoza-Yero, G. Minguez-Vega, L. Martinez-Leon, M. Carbonell-Leal, M. Fernandez-Alonso, C. Donate-Buendia, J. Perez-Vizcaino, and J. Lancis, "Diffraction-based phase calibration of spatial light modulators with binary phase Fresnel lenses," J. Disp. Technol. **12**, 1027–1032 (2016).
15. L. Martínez-León, Z. Jaroszewicz, A. Kołodziejczyk, V. Durn, E. Tajahuerce, and J. Lancis, "Phase calibration of spatial light modulators by means of Fresnel images," J. Opt. A **11**, 125405 (2009).
16. J. L. M. Fuentes, E. J. Fernández, P. M. Prieto, and P. Artal, "Interferometric method for phase calibration in liquid crystal spatial light modulators using a self-generated diffraction-grating," Opt. Express **24**, 14159–14171 (2016).
17. J. E. Wolfe and R. A. Chipman, "Polarimetric characterization of liquid-crystal-on-silicon panels," Appl. Opt. **45**, 1688–1703 (2006).
18. F. J. Martínez, A. Márquez, S. Gallego, M. Ortuño, J. Francés, A. Beléndez, and I. Pascual, "Averaged Stokes polarimetry applied to evaluate retardance and flicker in PA-LCoS devices," Opt. Express **22**, 15064–15074 (2014).
19. J. Xia, C. Chang, Z. Chen, Z. Zhu, T. Zeng, P. Y. Liang, and J. Ding, "Pixel-addressable phase calibration of spatial light modulators: a common-path phase-shifting interferometric microscopy approach," J. Opt. **19**, 125701 (2017).
20. G. Pedrini, H. Li, A. Faridian, and W. Osten, "Digital holography of self-luminous objects by using a Mach–Zehnder setup," Opt. Lett. **37**, 713–715 (2012).
21. K. Choi, J. Yim, and S.-W. Min, "Achromatic phase shifting self-interference incoherent digital holography using linear polarizer and geometric phase lens," Opt. Express **26**, 16212–16225 (2018).
22. K. Choi, J. Yim, S. Yoo, and S.-W. Min, "Self-interference digital holography with a geometric-phase hologram lens," Opt. Lett. **42**, 3940–3943 (2017).
23. Y. Dai, J. Antonello, and M. J. Booth, "Calibration of a phase-only spatial light modulator for both phase and retardance modulation," Opt. Express **27**, 17912–17926 (2019).
24. S. Mukhopadhyay, S. Sarkar, K. Bhattacharya, and L. Hazra, "Polarization phase shifting interferometric technique for phase calibration of a reflective phase spatial light modulator," Opt. Eng. **52**, 035602 (2013).
25. L. Yang, J. Xia, C. Chang, X. Zhang, Z. Yang, and J. Chen, "Nonlinear dynamic phase response calibration by digital holographic microscopy," Appl. Opt. **54**, 7799–7806 (2015).
26. J. Kim, Y. Li, M. N. Miskiewicz, C. Oh, M. W. Kudenov, and M. J. Escuti, "Fabrication of ideal geometric-phase holograms with arbitrary wavefronts," Optica **2**, 958–964 (2015).
27. K. Gao, H.-H. Cheng, A. K. Bhowmik, and P. J. Bos, "Thin-film Pancharatnam lens with low f-number and high quality," Opt. Express **23**, 26086–26094 (2015).
28. J. W. Goodman, *Introduction to Fourier Optics*, 4th ed. (W.H. Freeman, 2017).
29. B. Piccirillo, M. F. Picardi, L. Marrucci, and E. Santamato, "Flat polarization-controlled cylindrical lens based on the Pancharatnam–Berry geometric phase," Eur. J. Phys. **38**, 034007 (2017).
30. Sony, "Polarization Image Sensor," https://www.sony-semicon.co.jp/products/common/pdf/IMX250_253MZR_MYR_Flyer_en.pdf.
31. L. A. Alemán-Castaneda, B. Piccirillo, E. Santamato, L. Marrucci, and M. A. Alonso, "Shearing interferometry via geometric phase," Optica **6**, 396–399 (2019).
32. D. Malacara-Hernandez, *Optical Shop Testing* (John Wiley & Sons, 2007).
33. P. Hariharan and D. Sen, "Radial shearing interferometer," J. Sci. Instrum. **38**, 428–432 (1961).
34. Z. Cheng, D. Liu, Y. Yang, T. Ling, X. Chen, L. Zhang, J. Bai, Y. Shen, L. Miao, and W. Huang, "Practical phase unwrapping of interferometric fringes based on unscented Kalman filter technique," Opt. Express **23**, 107–117 (2015).
35. E. Stoykova and H. Kang, "Twin-image problem in digital holography—a survey," Chin. Opt. Lett. **12**, 060013 (2014).
36. K. Dabov, R. Foi, V. Katkovnik, and K. Egiazarian, "BM3D image denoising with shape-adaptive principal component analysis," in *Proc. Work. Signal Process. with Adapt. Sparse Struct. Represent.* (2009), Vol. **6**, pp. 1–7.
37. M. Lebrun, "An analysis and implementation of the BM3D image denoising method," Image Process. Line **2**, 175–213 (2012).
38. M. Cywińska, M. Trusiak, V. Micó, and K. Patorski, "Single-frame fringe pattern analysis using modified variational image decomposition aided by the Hilbert transform for fast full-field quantitative phase imaging," in *Unconventional Optical Imaging*, C. Fournier, M. P. Georges, and G. Popescu, eds. (SPIE, 2018), p. 82.
39. K. Falaggis, T. Kozacki, and M. Kujawinska, "Computation of highly off-axis diffracted fields using the band-limited angular spectrum method with suppressed Gibbs related artifacts," Appl. Opt. **52**, 3288–3297 (2013).
40. T. Kozacki, K. Falaggis, and M. Kujawinska, "Computation of diffracted fields for the case of high numerical aperture using the angular spectrum method," Appl. Opt. **51**, 7080–7088 (2012).
41. J. Xia, C. Chang, Z. Chen, Z. Zhu, T. Zeng, P. Y. Liang, and J. Ding, "Pixel-addressable phase calibration of spatial light modulators: a common-path phase-shifting interferometric microscopy approach," J. Opt. **19**, 125701 (2017).